PM2.5/PM10 Ratio Prediction Based on a Long Short-term Memory Neural Network in Wuhan, China

Xueling Wu [*], **Ying Wang, Siyuan He, Zhongfang Wu**

Institute of Geophysics and Geomatics, China University of Geosciences, Wuhan 430074, China

[*] Corresponding author. E-mail: snowforesting@163.com; Tel: +86-27-67883251; Fax: +86-27-67883251

Abstract

Air pollution is a serious and urgent problem in China, and it has a great impact on the lives of residents and urban development. The particulate matter (PM) value is usually used to indicate the degree of air pollution. In addition to PM2.5 and PM10, the use of the PM2.5/PM10 ratio as an indicator and assessor of air pollution has also become more widespread. This ratio reflects the air pollution conditions and pollution sources. In this paper, a better composite prediction system was proposed that aimed at improving the accuracy and spatio-temporal applicability of PM2.5/PM10. First, the aerosol optical depth (AOD) in 2017 in Wuhan was obtained based on Moderate Resolution Imaging Spectroradiometer images, with a 1 km spatial resolution, by using the Dense Dark Vegetation method. Second, the AOD was corrected by calculating the planetary boundary layer height and relative humidity. Third, the coefficient of determination of the optimal subset selection was used to select the factor with the highest correlation with PM2.5/PM10 from meteorological factors and gaseous pollutants. Then, PM2.5/PM10 predictions based on time, space, and random patterns were obtained by using 9 factors (the corrected AOD, meteorological data and gaseous pollutant data) with the long short-term memory (LSTM) neural network method, which is a dynamic model that remembers historical information and applies it to the current output. Finally, the LSTM model prediction results were compared and analysed with the results of other intelligent models. The results showed that the LSTM model had significant advantages in the average, maximum and minimum accuracies and the stability of PM2.5/PM10 prediction.

Keywords: Air pollution · PM2.5/PM10 · MODIS · AOD · LSTM

1. Introduction

Aerosols are a general term for solid and gas particles suspended in air. Aerosols can have an important impact on regional and global atmospheric environments, climates, and ecosystems and have long been an important issue in global environmental change research (Crutzen and Andreae, 1990). Particulate matter (PM) is usually separated and categorized based on its aerodynamic diameter, and the most widely monitored particles are PM10 and PM2.5. PM10 is primarily produced by natural processes, such as resuspending local soils, sandstorms, and roadside dust, and various industrial processes. Particles with an aerodynamic particle size not exceeding 2.5 μm are called fine PM (PM2.5), which mainly derive from anthropogenic emissions. Anthropogenic combustion products come from transportation and energy production and are particularly important for environmental policy and public health research (Pope and Dockery, 2006; Xie et al., 2011). Infectious disease research shows that there is a significant consistency between the PM2.5 environmental quality concentration and adverse effects on human health (Lelieveld et al., 2015). PM2.5 mainly causes damage to the respiratory and cardiovascular systems, including coughing, difficulty breathing, lowered lung function, and aggravated asthma, causing chronic bronchitis, arrhythmia, non-fatal heart disease, and premature death of patients with cardiopulmonary disease (Wu et al., 2011; Jia et al., 2012). In addition, since the scattering extinction contribution of PM2.5 particles accounts for 80% of the extinction of the atmosphere, the concentration of PM2.5 is a key factor in determining the visibility of the atmosphere. In view of the importance of aerosols and near-surface atmospheric PM2.5 to regional and global climates and environments, quantitative and accurate observations using a variety of observation methods have become a hot research topic domestically and internationally (Dominici et al., 2006). Since fine and coarse particles come from different sources, the PM2.5-PM10 scale model has different physicochemical properties, which can not only distinguish the type of aerosol in the PM but also provide the mixing ratio of dust and artificial aerosols (Sugimoto et al., 2015). For the research conducted in an urban area of northwestern China, PM10 and PM2.5 concentration data were collected to reveal the spatial-temporal behaviour of local PM and mineral dust fractions (Qingyu et al., 2018).

The aerosol optical depth (AOD) is defined as the integral of the extinction coefficient of a medium in the vertical direction, which describes the effect of aerosols on light reduction. A study conducted by Hidy in 2009 indicated that the estimation of the PM2.5 concentration near the ground by satellite remote sensing AOD has great research potential (Hidy, 2009). The advantage is that satellite remote sensing data are generally standardized data with high reliability and a wide spatial coverage, providing wide-area, spatially continuous and real-time monitoring information for regional and global PM2.5 air quality assessment. There are many ways to obtain the AOD from remote sensing data.

AOD products can be produced by many satellite sensors, such as the Geostationary Operational Environmental Satellite (GOES) (Prados et al., 2007), Advanced Very High Resolution Radiometer (AVHRR) (Gao et al., 2016), and Moderate Resolution Imaging Spectroradiometer (MODIS) (Levy et al, 2013). MODIS data are one of the most widely used data sources for deriving ground PM2.5 concentrations with AOD (Hu et al., 2014). There are many ways to obtain AOD through MODIS data. For example, Yang et al. used the data collected by Landsat 8 satellite images to retrieve the AOD in Beijing by means of the Dark Target method and the visible near-infrared atmospheric correction method. The accuracy was verified by the Aerosol Robotic Network (AERONET) observation data (Ou et al., 2017). The Dark Blue AOD retrieval method was used to complement the Dark Target results by retrieving the AOD over bright arid land surfaces, such as deserts (Sayer et al., 2013). In addition, a new method that considers bidirectional reflectance of the surface was proposed, which is suitable for calculating the AOD in arid or semi-arid regions (Xinpeng et al., 2018).

Although the relationship between the AOD and PM has been proven by many scholars, since the PM concentration level is usually measured at the surface, the correlation between them is affected by the planetary boundary layer height (PBLH) and relative humidity (RH). When studying the seasonal PM10-AOD correlation in northern Italy, Arvani et al. found that the introduction of PBLH and RH correction can significantly improve the bin-averaged PM AOD correlation (Arvani et al., 2016). After the vertical and RH correction methods were applied to the air quality station in Beijing, the determination coefficient R^2 of the AOD and PM10 increased by 0.13, and the correlation between the AOD and PM2.5

increased from 0.48 to 0.62 (Wang et al., 2010). These calibration methods usually require the use of meteorological data to perform the calculation, and the addition of meteorological data to the evaluation of PM concentration can give better results. For instance, Jung et al. joined meteorological data to obtain an improved model of the surface PM2.5 from 2005 to 2015 to estimate the PM concentration for the entire main island of Taiwan (Jung et al., 2017).

Many statistical models have been used for the ground PM estimation of AOD and other predictors, such as linear regression models, random forest models, neural network models, and generalized additive models. However, with the introduction of new intelligent models, the traditional regression model reflects the inability to balance time, space and random precision. One way to overcome these limitations is the long short-term memory (LSTM) model. The LSTM network is ideal for learning from experience so that time series can be classified, processed, and predicted with very long unknown time lags between important events. In the study of PM2.5 monitoring and prediction in smart cities, Chiou-Jye et al. proposed that the prediction accuracy of the convolutional neural network (CNN)-LSTM model is the highest compared to the prediction accuracies of several other classic machine learning methods (Chiou-Jye and Ping-Huan, 2018). Xiang et al. used the LSTM model to automatically extract inherent useful features from historical air pollutant data to obtain a more efficient multi-scale prediction framework (Li et al., 2017).

This paper used a total of 59 AOD results for all of 2017 by the Dense Dark Vegetation (DDV) method using MODIS level-2 data of Wuhan with a spatial resolution of 1 km. Since there were only 10 air quality stations in Wuhan, to ensure accuracy, the AOD values were extracted at the air quality station site, and the integration of the AOD, air pollutants, and meteorological data was also based on the station site. AOD* was obtained by correcting AOD using the PBLH and RH. Then, the R^2-based optimal subset selection method was used to select the most relevant factor for PM2.5/PM10 from the meteorological factors and air pollutants. Finally, the space and time scales and random PM2.5/PM10 predictions were determined and performed, respectively, via the LSTM model, and the prediction results of the LSTM model and other classic models were compared and analysed.

2. Study area

Wuhan is the provincial capital of Hubei Province. The administrative extent is between 113.683°E-115.083°E and 29.967°N-31.367°N, and the total area is 8494.41 km^2 (Zhou and Chen, 2018). The largest distance is between the eastern and western parts of Wuhan and is 134 km, and the maximum distance from north to south is 155 km. Wuhan is the city with the largest population, is the largest provincial capital city, has the most complicated road traffic and has the most developed economy in the central part of the country (Jiao et al., 2017). The Yangtze River flows through Wuhan, and there are hundreds of lakes in Wuhan. The terrain of Wuhan is mainly plains, with low levels in the middle of the region and low mountains, hills and ridges to the south and north. The climate type is a humid, north subtropical monsoon climate with high temperatures in summer, low temperatures in winter, and an annual average temperature of 15.9 °C. Sunshine hours and total radiation are also at high levels, and the annual average precipitation is approximately 1300 mm. June and August receive the most precipitation in Wuhan, and summer precipitation accounts for approximately 40% of the annual rainfall. In recent years, the air quality in Wuhan has been improved. In 2017, the number of days in which the annual air quality level was acceptable was 255 days, and the acceptability rate was 69.9%. At the same time, the number of days with light pollution, moderate pollution, heavy pollution, and severe pollution was 86 days, 17 days, 6 days, and 1 day, respectively.

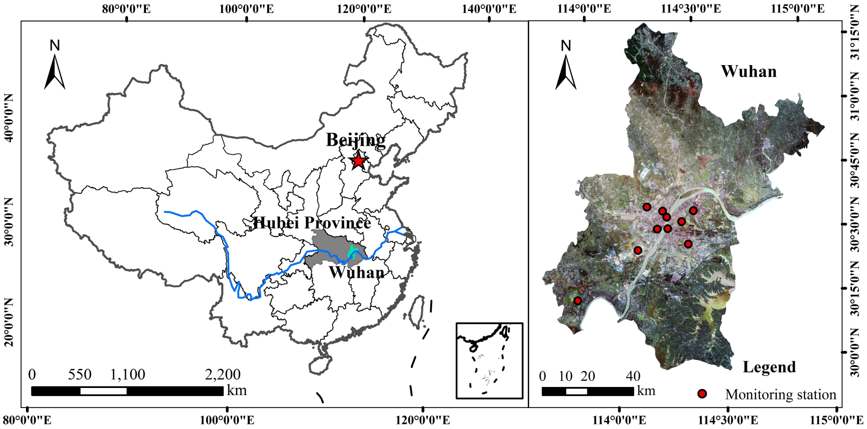

(A) (B)

Fig. 1 Location of the study area in China (A: map of China, B: map of Wuhan).

3. Methods

The data that our environmental monitoring station can monitor are only real-time data. If we want to predict the state of the air afterwards, we can use other relevant factors for reference. The AOD is an important parameter in the study of atmospheric aerosols, which have a great relationship with PM. Gaseous pollutants are also a key factor in air quality. In addition, changes in meteorological conditions have an impact on PM. Therefore, we used the air quality data from the ground monitoring station as the inspection standard and extracted the values of these correlation factors with the data from the monitoring site for verification. After retrieving the AOD with the MODIS images, the AOD values at the monitoring site were extracted, and the values of the meteorological data were also interpolated at the same point. Then, the AOD was corrected to obtain the AOD*, and gaseous pollutant data at the monitoring site were added. The best set that predicted air quality was selected, and machine learning techniques were used to obtain models that can make space and time series predictions (Fig. 2).

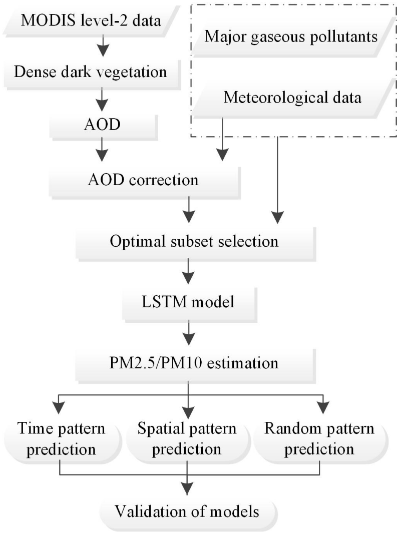

Fig. 2 A flow chart of the research process.

3.1 AOD retrieval

MODIS is an important sensor on the Terra and Aqua satellites. The Terra satellite is a morning star, passing from north to south at approximately 10:30, and Aqua acts as an afternoon star, moving from south to north at 13:30. Wuhan is located in the central and eastern parts of Hubei Province at the southeast corner of the h27v05 frame; therefore, we chose to use the images collected by Terra because of its higher image quality. The MODIS data have 36 spectral bands, ranging from 0.4 μm to 14.4 μm, of which 7 bands can be used to retrieve the AOD, while the best bands for over-land aerosol retrieval are 0.47 μm, 0.66 μm, and 2.12 μm, especially in areas with dense vegetation. We downloaded the MOD02_L1B data for the region in Wuhan in 2017 via the website (https://ladsweb.modaps.eosdis.nasa.gov) and removed a number of days with a large amount of clouds, finally obtaining 59 images with a spatial resolution of 1 km. According to the DDV method (Li et al., 2014), after radiation correction, geometric correction, angle data resampling, and angle data geometric correction and synthesis, cloud detection processing was performed; then, a lookup table file was generated according to the "6S" atmospheric radiation model, and the AOD was acquired (Fig. 3). After verifying with the MOD04_L2 aerosol product data released by the National Aeronautics and Space Administration (NASA), the results of the retrieval were considered valid and used later. Fig. 4 shows the results of the AOD retrieval on July 18th.

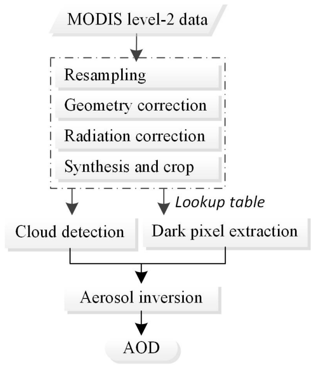

Fig. 3 A flow chart of the AOD retrieval.

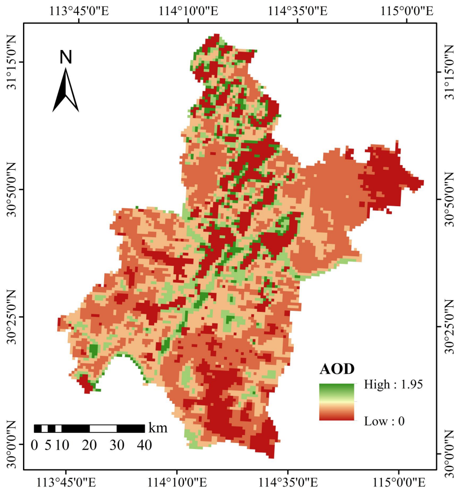

Fig. 4 AOD retrieval on July 18th.

3.2 Ground-level air quality and gaseous pollutant data

The Ministry of Ecology and Environment of China has established 10 national environmental quality control stations in Wuhan. The shortest distance between points exceeds 3 km, and the average distance exceeds 10 km. Each station continuously collects hourly average concentration values of PM2.5, PM10, SO_2, NO_2, O_3, and CO and publishes the daily average concentration values. The calculations in this paper were based on these daily averaged data. The monthly average concentration data of PM2.5, PM10, and gaseous pollutants obtained from these data in 2017 are shown in Table 1. During the year, the trends in PM2.5 and PM10 were roughly the same. From February to April, the values dropped rapidly. From April to May, both experienced a small increase, and there were decreases from May to July. The concentration of PM2.5 continued to rise after July, and the growth rate became larger. The concentration of PM10 also increased after July but decreased between September and October. NO_2 is mainly derived from the high-temperature combustion process of fossil fuels. The combustion of nitrogen-containing fuels (such as coal) and nitrogen-containing chemicals can directly release NO_2. In general, motor vehicle emissions are one of the main sources of urban NO_2. SO_2 is a ubiquitous pollutant in cities. The SO_2 in the air mainly comes from the industrial production of thermal power generation and other industries, such as the combustion of fixed-source fuels; the production of non-ferrous metals; the production of steel, chemical, and sulfur plants; and discharge from small heating boilers and civil coal furnaces. Natural processes, such as volcanic activity, also emit a certain amount of SO_2. CO is a colourless, odourless, flammable, and toxic gas that is a product of the incomplete combustion of carbonaceous fuels. The concentrations of SO_2, NO_2, and CO showed regularity. The concentration in summer was the lowest, followed by spring and autumn, and the highest was in winter. The lowest value was in June or July, and the highest was in December. O_3 is a representative pollutant for photochemical smog, which is formed and enriched by nitrogen oxides and hydrocarbons in the air under intense sunlight and through a series of complex atmospheric chemical reactions. Although O_3 in the upper stratosphere has important anti-radiation protection for life on Earth's, O_3 at low altitudes in cities is a very harmful pollutant. The trend in the O_3 concentration was different, where the winter value was low and then increased in spring with time. In summer, the O_3 concentration fluctuated at a higher level and decreased in autumn.

Table 1 Monthly average concentrations of PM2.5, PM10, and gaseous pollutants in 2017.

Month	PM2.5 (μg/m^3)	PM10 (μg/m^3)	SO_2 (μg/m^3)	NO_2 (μg/m^3)	O_3 (μg/m^3)	CO (mg/m^3)
Jan	99.48	147.26	26.66	48.20	36.86	1.40
Feb	121.17	167.42	16.63	46.01	36.13	1.44
Mar	59.44	145.11	27.04	51.88	60.96	1.11
Apr	41.27	93.87	16.07	38.35	93.18	0.93
May	52.85	107.95	12.00	40.15	125.30	0.93
Jun	27.80	55.35	4.82	25.45	102.20	0.81
Jul	24.23	53.13	6.05	17.77	107.92	0.62
Aug	27.37	65.09	11.07	24.47	73.24	1.04
Sep	36.20	87.85	19.11	40.55	139.25	1.33
Oct	39.07	77.20	13.65	43.64	54.00	1.10
Nov	90.88	134.91	21.53	62.36	54.28	1.19
Dec	111.15	148.29	27.06	70.21	21.78	1.50

3.3 Meteorological data

The quality of air is closely related to meteorological conditions. The meteorological data obtained in this paper derive from the National Meteorological Information Center of China's National Meteorological Information Network (http://data.cma.cn/site/index.html) and includes average rainfall, evaporation capacity, RH, sunshine intensity, average surface temperature, average wind velocity, average air pressure, and average temperature. The data obtained were daily average data in 2017. A total of 5 meteorological stations exist near the Wuhan area. To obtain meteorological data near the air quality monitoring stations, data from the meteorological stations needed to be interpolated. After comparing the kriging, natural neighbour, spline, and inverse distance weighted methods, we found that the results acquired by setting 12 interpolation points and using the spherical model of the kriging method were more suitable for the study area. The kriging method is a multi-step process that includes the exploratory statistical analysis of the data, the modelling of variograms, the creation of surfaces, and the study of varying surfaces. The monthly averages of the meteorological data at all of the calculated sites are shown in Table 2. The seasonal changes reflected by several meteorological data results were more obvious. The average surface temperature and average temperature showed a higher trend in summer and a lower trend in winter. The average air pressure had a completely opposite trend. The sunshine intensity and evaporation capacity were lower in winter and fluctuated in the other three quarters. The rainfall was concentrated in summer and autumn, while the average wind velocity and RH had no obvious seasonal characteristics.

Table 2 Monthly averages of the meteorological data.

Month	Average rainfall (0.1 mm)	Evaporation capacity (0.1 mm)	Average surface temperature (0.1℃)	Average air pressure (0.1 hPa)	Relative humidity (-1%)	Sunshine intensity (0.1 h)	Average temperature (0.1℃)	Average wind velocity (0.1 m/s)
Jan	0.00	18.09	62.19	10230.27	63.91	58.06	47.78	16.51
Feb	38.84	19.55	108.27	10151.31	72.03	24.23	103.45	29.35
Mar	0.00	29.34	140.11	10166.74	64.14	94.10	115.67	14.52
Apr	0.00	35.81	211.98	10103.29	69.60	105.93	181.67	16.16
May	0.00	36.81	288.18	10062.96	66.83	103.69	240.91	10.72
Jun	30.49	37.48	289.44	10002.23	84.54	64.80	261.32	18.69

Jul	2.33	57.25	366.30	10011.06	70.70	112.87	317.36	22.14
Aug	24.15	37.88	318.01	10017.01	81.09	84.67	296.38	18.88
Sep	0.00	45.47	289.04	10093.00	69.64	106.04	242.16	19.61
Oct	20.54	19.50	199.33	10138.21	84.03	61.31	176.99	11.60
Nov	0.00	21.36	157.65	10180.33	75.21	85.71	131.89	13.28
Dec	0.00	15.80	59.94	10222.16	67.78	76.57	42.91	9.12

4. Methods

4.1 AOD correction

The PBLH refers to the thickness of the planetary boundary layer and is an important physical parameter for numerical atmospheric models and environmental evaluations (Su et al., 2018). The PBLH is calculated by a commonly used national standard method in China. The national standard method is performed according to the method specified in the Chinese national standard GB/T13201-91. This method assumes that the thermal conditions of the near-surface layer depend, to a large extent, on the degree of ground heating and cooling. This method takes into account the thermal and dynamic factors and quantifies the solar elevation angle, cloud volume, and wind speed. Then, according to the specified local parameters, the atmospheric stability is classified into A, B, C and D categories according to the Pasquill stability classification:

$$h = \frac{a_s U_{10}}{f} \tag{1}$$

When the atmospheric stability is E and F:

$$h = \frac{b_s \sqrt{U_{10}}}{f} \tag{2}$$

$$f = 2\Omega \sin\varphi \tag{3}$$

where *h* (m) is the thickness of the mixing layer; U_{10} (m*s^{-1}) is the average wind velocity at a height of 10 m, which is 6 m*s$^{-1;}$, a_s and b_s are the mixing layer coefficients; *f* is the ground rotation parameter; Ω is the ground rotation angular velocity, with a value of 7.29×10^{-5} rad*s^{-1}; and φ (°) is the geographic latitude.

The aerosol hygroscopic growth factor f(RH), where RH is the relative humidity, describes the extent to which the aerosol extinction cross section or scattering coefficient increases with increasing RH, depending on a variety of factors, such as the temperature absorption properties of the aerosol (Cai et al., 2018). The common formula for calculating f(RH) is:

$$f(RH) = 1/(1 - RH/100) \tag{4}$$

Since the parameters describing atmospheric physical conditions, such as air pressure, atmospheric temperature and atmospheric humidity change, exist much more in the vertical than horizontal direction, it is often assumed that the atmosphere has a structure in which the horizontal direction is uniform, and the vertical direction is layered. For the single homogeneous distribution of spherical aerosol particles, the near-surface particle concentration can be obtained by measuring a dry air sample. The expression is as follows:

$$PM = \frac{4}{3}\pi\rho\int r^3 n(r)dr \tag{5}$$

where ρ (g/m^3) is the average density of the particles and $n(r)$ is the particle spectral distribution function under ambient humidity, which is related to the particle size.

Given the wavelength of the radiation, the aerosol optical thickness from the ground to a height of H can be expressed as:

$$AOD = \pi\int_0^H\int_0^\infty Q_{ext,amb}(r)n_{amb}(r)r^2 drdz \tag{6}$$

To convert $Q_{ext,amb}$ under ambient humidity to $Q_{ext,dry}$ under dry conditions, a hygroscopic growth factor f(RH) is required. This factor represents the ratio of normalized particle scattering efficiency under ambient RH and dry conditions and is a function of humidity:

$$AOD=\pi f(RH)\int_0^H\int_0^\infty Q_{ext,dry}(r)n(r)r^2drdz \tag{7}$$

A normalized particle scattering efficiency Q_{ext} and a parameterized expression of the effective radius r_{eff} are introduced for replacement in the above formula:

$$Q_{ext}=\frac{\int r^2Q_{ext}(r)n(r)dr}{\int r^2n(r)dr} \tag{8}$$

$$r_{eff}=\frac{\int r^3(r)n(r)dr}{\int r^2n(r)dr} \tag{9}$$

Finally, the relationship between the AOD and near-surface PM2.5 mass concentration is introduced:

$$AOD=PM2.5Hf(RH)\frac{3Q_{ext,dry}}{4\rho r_{eff}}=PM2.5HS \tag{10}$$

where S (m^2g^{-1}) represents the specific extinction efficiency of the aerosol under ambient humidity conditions. H stands for aerosol elevation. In practice, the PBLH approximation is often used instead of H. According to the above relationship between the AOD and PM2.5, it can be inferred that if the AOD is corrected by the factors PBLH and f(RH), the corrected AOD*, that is, AOD/(PBLH*f(RH)), is expected to have better correlation with PM. Taking the monthly average value as an example, the parameters PBLH and f(RH) used by the AOD correction algorithm and the corrected AOD* are shown in Table 3. The monthly average data of PM2.5/PM10, AOD and AOD* are shown in Fig. 5. In fact, after calculating the linear correlations of the AOD and AOD* with PM2.5/PM10, the correlation increased from 0.838 to 0.873.

Table 3 Monthly average AOD, PBLH, f(RH), and AOD*.

Month	AOD ($\times10^{-1}$)	PBLH	f(RH)	AOD* ($\times10^{-4}$)
Jan	12.610	428	4.00	7.366
Feb	12.343	444	3.85	7.221
Mar	9.200	461	4.00	4.989

Apr	5.192	713	4.00	1.820
May	5.625	686	4.00	2.050
Jun	4.000	631	5.00	1.268
Jul	3.895	686	5.56	1.021
Aug	5.083	686	5.26	1.409
Sep	6.375	741	4.35	1.978
Oct	4.964	395	4.00	3.142
Nov	10.06	412	3.85	6.345
Dec	15.263	412	3.57	10.377

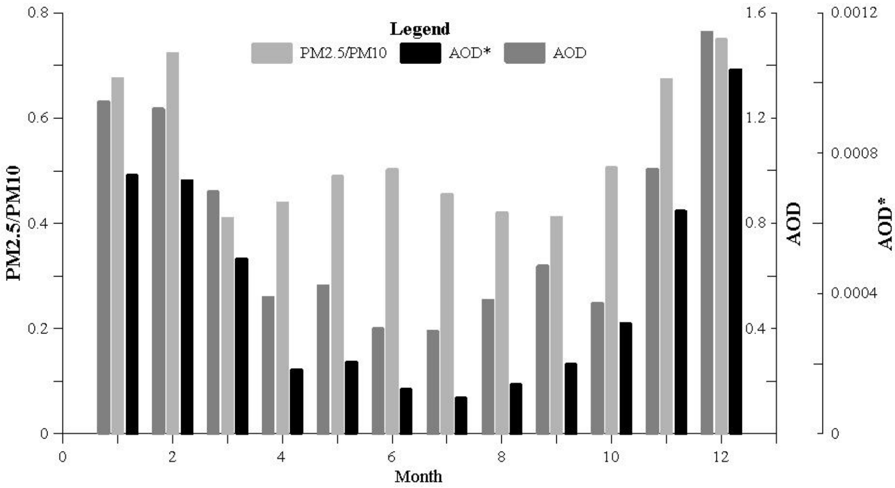

Fig. 5 A bar chart of monthly average PM2.5/PM10, AOD and AOD*.

4.2 Selection factors

When choosing a subset, the choice of independent variables should be practical. How to choose the best subset of variables to establish a better regression equation has been a hot research topic. An optimal way to choose a regression equation is to combine all of the independent variables with the dependent variable to establish all possible equations and then select one of the best-performing subsets from all possible equations. This is called the optimal subset method. The optimal subset method can determine an optimal regression equation from all possible subsets via some criteria and has been widely used in weather and climate predictions. Using the correlation coefficient R^2 as the evaluation index and the optimal subset of PM2.5/PM10 as the dependent variable, the highest R^2 is 0.461. The independent variables in the subset are AOD*; average rainfall; evaporation capacity; RH; sunshine intensity; average wind velocity; and SO_2, CO, and O_3 concentrations. The factors selected by the optimal subset method are shown in Table 4. The symbol "√" indicates that the factor is selected.

Table 4 Factors selected by the optimal subset method.

R^2 Factors	0.461	0.460	0.460	0.457	0.455	0.455	0.454	0.453	0.452	0.452
CO	√	√	√	√	√	√	√	√	√	√
Average rainfall	√	√	√	√	√		√	√	√	√
Evaporation capacity	√	√	√	√	√	√	√	√	√	√
Relative humidity	√	√	√		√		√	√	√	√
Sunshine intensity	√	√	√	√	√	√	√	√		√
Average wind velocity	√	√		√	√	√	√	√	√	√
AOD*	√	√	√	√	√	√	√	√	√	√
SO_2	√	√	√	√	√	√	√	√	√	√
O_3	√	√	√	√	√	√	√	√	√	√
Average air pressure		√		√	√	√				
Average surface temperature				√	√	√				√
Average temperature							√			
NO_2								√		

4.3 RNNs and the LSTM model

The recurrent neural network (RNN) is a powerful deep neural network that uses its internal memory to process input sequences with any timing. In the RNN model, compared with the common multi-layer neural network, the interconnection layer is added between the nodes of the hidden layer, and the directional loop is formed by the connection between the hidden layer neural units; then, the internal state of the network is created, and the dynamic time series behaviour is presented (Bao and Zeng, 2013). The RNN can handle any sequence length in principle, but in an actual situation, the standard RNN model cannot store sequence information about the past and lacks the ability to establish remote structure connections. This kind of "forgetting" limitation cannot record long-term information. Thus, these networks are more prone to instability when generating sequences, resulting in a time dependency problem. This problem is not unique to RNNs but exists in almost all generation models. The LSTM model is a network that is used to address long-term time-dependent dependencies. It is a time-RNN suitable for processing and predicting important events with relatively long intervals and delays in time series (Weninger et al., 2014).

The key to distinguishing the LSTM model from the traditional RNN is that the traditional RNN has only one hidden layer output value state *h*, and *h* changes with the convolution process and is insensitive to long-term or long-distance events. The LSTM model adds a unit state *c* to store the long-term status. The calculation process after adding *c* is shown in Fig. 6:

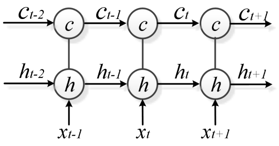

Fig. 6 The calculation process of unit *c* in the LSTM model.

where *x*, *h*, and *c* are vectors. At time *t*, there are three inputs to the LSTM: the input value x_t of the current time network, the output value h_{t-1} of the LSTM model at the previous time, and the unit state c_{t-1} of the previous time. The two outputs of the LSTM are the current time LSTM output value h_t and the current state of the unit c_t.

The key point of the LSTM model is how to control the state *c*. The idea of the LSTM model is to use three control switches to control it. The first switch control continues to store *c*, the second switch control inputs the current state to *c*, and the third switch controls whether *c* is the current output of the LSTM model. The switches implemented in the algorithm are known as "gates", which are fully connected layers whose input is a vector, and the output is a real vector between 0 and 1 (Srivastava and Lessmann, 2018). Assuming *W* is the weight vector of a gate and *b* is the bias value, then the gate can be expressed as:

$$g(x) = s(Wx + b) \tag{11}$$

These three gates are defined as follows:

$$i_t = \sigma(W_i * [h_{t-1}, x_t] + b_i) \tag{12}$$

$$f_t = \sigma(W_f * [h_{t-1}, x_t] + b_f) \tag{13}$$

$$o_t = \sigma(W_o * [h_{t-1}, x_t] + b_o) \tag{14}$$

where i_t, f_t, and o_t are the values of the input, forget, and output gates, respectively; σ is the activation function; and b_i, b_f, and b_o are their respective bias values. The structure of the LSTM model is shown in Fig. 7. The inputs are in terms of time, space and randomness, and the outputs are their results.

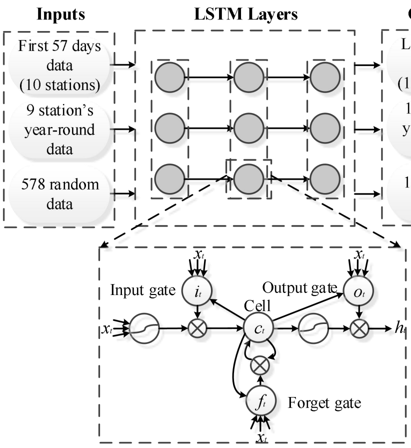

Fig. 7 Architecture of the LSTM model.

5. Results and discussion

To determine the appropriate number of layers for the LSTM method, we divided the training data set into two parts: 80% of the data were used as the training sample for modelling, and 20% of the data were used as the verification sample. We tried to use various layers for the comparison. After obtaining the results of various layers, we found that the results obtained using the four-layer LSTM structure were the best, with the first three layers being the LSTM layer and the last layer being the dense layer. Because the LSTM uses the activation function as the gate, the outputs of the gates must be between 0 and 1, and the output ranges of both types of activation functions must be satisfied. We determined that the activation function for setting the forget gate and the input gate was defined as a sigmoid function. The best activation function for outputting the results was the tanh function.

5.1 Time pattern prediction

Using the input of the first 57 days in the 2017 data from 10 sites, there were 570 input samples, and the data used to verify the model were from the last two days in 2017. These two days were December 25 and December 31. In winter, with a high PM2.5/PM10 value, the ratios were more concentrated above 0.6. We compared the prediction results of the LSTM model with the multi-layer perceptron (MLP), back propagation (BP) artificial neural network, support vector machine (SVM), and chi-squared automatic interaction detector (CHAID) decision tree models. Then, we calculated the error rate between the predicted value and the measured value (Table 5). Among the five algorithms, the average error of the LSTM model was the smallest, 15.1704, and its minimum error was also the smallest, only 0.877, but its maximum error value was larger than the BP and SVM maximum errors values. The MLP method had the worst predictions, whether in terms of the average error, maximum error or minimum error. It seemed that the MLP method was not suitable for predictions in terms of air quality time series. The BP network method and the SVM had similar prediction results; the average error was not too large, and the maximum error value was smaller than that of the LSTM, while the minimum error value was larger. Although the average error of the CHAID model was small, the minimum error and the maximum error values were both bad. None of the five prediction methods could accurately predict the case where the

PM2.5/PM10 value was greater than 0.9. The maximum value that the LSTM was able to predict was 0.8848. The predicted maximum values of the MLP, BP, SVM, and CHAID were 0.7606, 0.8321, 0.8568, and 0.8206, respectively.

Table 5 The results and relative error rates of the time pattern predictions.

Measured value	Predicted value					Relative error rate (%)				
	LSTM	MLP	BP	SVM	CHAID	LSTM	MLP	BP	SVM	CHAID
0.8212	0.7682	0.7329	0.7786	0.6698	0.4853	6.4540	10.7526	5.1875	18.4364	40.9036
0.7436	0.6910	0.6526	0.6961	0.7841	0.4853	7.0737	12.2378	6.3878	5.4465	34.7364
0.6629	0.5962	0.4624	0.7074	0.8353	0.6753	10.0618	30.2459	6.7129	26.0069	1.8706
0.6950	0.6297	0.5955	0.6850	0.5628	0.6753	9.3957	14.3165	1.4388	19.0216	2.8345
0.7816	0.6102	0.5134	0.6871	0.8092	0.5145	21.9294	34.3142	12.0906	3.5312	34.1735
0.6311	0.6795	0.6608	0.5864	0.7032	0.6487	7.6691	4.7061	7.0829	11.4245	2.7888
0.7959	0.4918	0.5211	0.6870	0.8568	0.6973	38.2083	34.5270	13.6826	7.6517	12.3885
0.8743	0.8487	0.7104	0.6474	0.7451	0.6973	2.9281	18.7464	25.9522	14.7775	20.2448
0.7204	0.4774	0.6087	0.8106	0.7446	0.8206	33.7313	15.5053	12.5208	3.3592	13.9089
0.9854	0.6031	0.7445	0.7154	0.6760	0.8206	38.7964	24.4469	27.4000	31.3984	16.7242
0.7079	0.7842	0.7606	0.8321	0.6089	0.7959	10.7784	7.4446	17.5449	13.9850	12.4311
0.9455	0.7127	0.7531	0.7064	0.7285	0.7959	24.6219	20.3490	25.2882	22.9508	15.8223
0.7200	0.4969	0.4701	0.6692	0.8172	0.6931	30.9861	34.7083	7.0556	13.5000	3.7361
0.8600	0.8848	0.5717	0.6192	0.6907	0.6931	2.8837	33.5233	28.0000	19.6860	19.4070
0.6571	0.6311	0.6055	0.7011	0.8522	0.5812	3.9568	7.8527	6.6961	29.6911	11.5508
0.9189	0.6849	0.6583	0.6195	0.7146	0.5812	25.4652	28.3600	32.5824	22.2331	36.7505
0.7640	0.7573	0.5281	0.6549	0.5406	0.7870	0.8770	30.8770	14.2801	29.2408	3.0105
0.9273	0.7777	0.5247	0.6354	0.7155	0.7870	16.1329	43.4164	31.4785	22.8405	15.1299
0.6277	0.6417	0.7458	0.7308	0.5392	0.6951	2.2304	18.8147	16.4250	14.0991	10.7376
0.8896	0.8075	0.6556	0.6685	0.6694	0.7534	9.2289	26.3040	24.8539	24.7527	15.3103
Mean:						15.1704	22.5724	16.1330	17.7017	16.2230
Maximum:						38.7964	43.4163	32.5824	31.3984	40.9036
Minimum:						0.8770	4.7061	1.4388	3.3592	1.8706

5.2 Spatial pattern prediction

One station was used as the output to be predicted; the other nine sites were inputs, and the prediction results of the spatial pattern were obtained. The output site is located in the southwest corner of Wuhan, which is the farthest from the other stations, and the distance from the nearest station is 34.7 km. The relative error rates of the predicted results of the five models are shown in Table 6. The average error rate of the LSTM model was still the lowest, along with the maximum error value, which was much smaller than that of the other models. The minimum error rate of the LSTM model was 0.1545%, which was not the lowest but was much smaller than the results of the SVM and CHAID model. In addition, we also conducted experiments using one station located in the central area of Wuhan as the output. The results of the LSTM model showed that the prediction results at this point were much better than those at the southwest point, and the average error rate was 25.1664%.

Table 6 The results and relative error rates of the spatial pattern prediction.

Models	LSTM	MLP	ANN	SVM	CHAID
Mean:	32.1585	37.6755	34.1333	34.0207	33.7718
Maximum:	160.3270	216.3275	222.9295	204.7317	230.1367
Minimum:	0.1545	0.1451	0.1124	0.9026	0.2396

5.3 Random pattern prediction

The random pattern prediction randomly selected 12 data points as the outputs among all 590 data points. The randomly selected measured data ranged from 0.2222 to 0.9843, covering the entire range of monitored values. After calculating the prediction results and relative error rates of the five models, the average, maximum and minimum error rates of the LSTM model were the smallest, and the results were significantly better than those of the other methods (Table 7). The predictions for the maximum and minimum values were also relatively good. However, it could be found that the prediction results obtained by these models were concentrated between 0.35 and 0.75, and the prediction results of the minimum and maximum values were generally poor.

Table 7 The results and relative error rates of the random pattern prediction.

Measured value	Predicted value					Relative error rate (%)				
	LSTM	MLP	BP	SVM	CHAID	LSTM	MLP	BP	SVM	CHAID
0.5870	0.5723	0.5443	0.5762	0.6091	0.4928	2.5043	7.2743	1.8399	3.7649	16.0477
0.6213	0.7449	0.6402	0.6561	0.6826	0.6795	19.8938	3.0420	5.6012	9.8664	9.3675
0.9843	0.6650	0.4874	0.6247	0.6185	0.7422	32.4393	50.4826	36.5336	37.1635	24.5962
0.8000	0.6238	0.4500	0.4772	0.5231	0.4928	22.0250	43.7500	40.3500	34.6125	38.4000
0.4638	0.4656	0.4773	0.4773	0.5136	0.4928	0.3881	2.9107	2.9107	10.7374	6.2527
0.7010	0.6913	0.5697	0.6811	0.6675	0.6795	1.3837	18.7304	2.8388	4.7789	3.0670
0.2222	0.3502	0.5598	0.4292	0.3971	0.3737	57.6058	151.9352	93.1593	78.7129	68.1818
0.5929	0.7606	0.6807	0.6543	0.6598	0.6795	28.2847	14.8086	10.3559	11.2835	14.6062
0.9571	0.5940	0.5346	0.6246	0.6698	0.6164	37.9375	44.1438	34.7404	30.0178	35.5971
0.7576	0.7611	0.6095	0.5959	0.6398	0.4928	0.4620	19.5486	21.3437	15.5491	34.9525
0.6277	0.6921	0.5654	0.6935	0.6802	0.6795	10.2597	9.9251	10.4827	8.3639	8.2523
0.8896	0.6743	0.5290	0.7551	0.7353	0.7422	24.2019	40.5351	15.1192	17.3449	16.5692
Mean:						19.7821	33.9239	22.9396	21.8496	22.9909
Maximum:						57.6058	151.9352	93.1593	78.7129	68.1818
Minimum:						0.3881	2.9107	1.8399	3.7649	3.0670

6. Conclusions

AOD inversion based on remote sensing technology is being increasingly used for air quality research and is important for monitoring and predicting air quality at a large scale. The proposed PM2.5/PM10 ratio reflects the air quality and impact of human activities, which is strongest in winter and summer and weakest in spring and autumn. In this paper, we used the DDV method to invert the 59 AOD data points in Wuhan in 2017 based on MODIS images. After the AOD was corrected by the PBLH and RH, the AOD*, which had a greater correlation with PM2.5/PM10, was obtained, which indicated that the method of correction with the PBLH and RH was effective. After combining gas pollutants and meteorological data, the optimal subset method was used to find the set of factors that were most suitable for the prediction of PM2.5/PM10. Since the LSTM model uses the gates as switches, better PM2.5/PM10 prediction results can be obtained. We hope to obtain a model that can predict air pollution anytime and anywhere by means of relative factors. Therefore, we set up three prediction patterns: time, space and random patterns. Among the five intelligent models for comparison, the LSTM model was the most effective, followed by the SVM model, and the CHAID decision tree model was the least effective. The relatively good results of the LSTM model were reflected not only in a higher average prediction accuracy but also in the better prediction of maximum and minimum values. Moreover, the accuracy of the LSTM model was more stable. However, the predictions for the maximum and minimum values were always below average, which will be the next focus of improvement.

Code availability Code content can be accessed through the following website: https://data.mendeley.com/datasets/zk9k53zw3z/1

Data availability Experimental data can be accessed through the following website: https://data.mendeley.com/datasets/zk9k53zw3z/2

Author contribution All authors worked collectively. Xueling Wu contributed to the conception of the study; Ying Wang contributed to analysis and manuscript writing; Siyuan He helped perform the analysis with constructive discussions; Zhongfang Wu performed the data analyses.

Competing interests The authors declare that they have no conflict of interest.

Acknowledgements This study was jointly supported by the National Natural Science Foundation of China (41871355 and 41571438).

References

1. Crutzen, P. J. , and Andreae, M. O.: Biomass burning in the tropics: impact on atmospheric chemistry and biogeochemical cycles. Science, 250(4988), 1669-1678, 1990.

2. Pope, C. A. , and Dockery, D. W.: 2006 Critical Review -- Health effects of fine particulate air pollution: lines that connect. Journal of the Air and Waste Management Association, 56(6), 709-742, 2006.

3. Xie, P. , Liu, X. , Liu, Z. , Li, T. , Zhong, L. , and Xiang, Y.: Human health impact of exposure to airborne particulate matter in pearl river delta, China. Water, Air and Soil Pollution, 215(1-4), 349-363, 2011.

4. Lelieveld, J. , Evans, J. S. , Fnais, M. , Giannadaki, D. , and Pozzer, A.: The contribution of outdoor air pollution sources to premature mortality on a global scale. Nature, 525(7569), 367-371, 2015.

5. Wu, S. , Deng, F. , Niu, J. , Huang, Q. , Liu, Y. , and Guo, X.: Exposures to PM2.5 components and heart rate variability in taxi drivers around the Beijing 2008 Olympic games. Science of the Total Environment, 409(13), 2478-2485, 2011.

6. Jia, X. , Song, X. , Shima, M. , Tamura, K. , Deng, F. , and Guo, X.: Effects of fine particulate on heart rate variability in Beijing: a panel study of healthy elderly subjects. International Archives of Occupational and Environmental Health, 85(1), 97-107, 2012.

7. Dominici, F. , Peng, R. D. , Bell, M. L. , Pham, L. , Mcdermott, A. , and Zeger, S. L. , et al.: Fine particulate air pollution and hospital admission for cardiovascular and respiratory diseases. JAMA, 295(10), 1127-1134, 2006.

8. Sugimoto, N., Shimizu, Atsushi, Matsui, I.: A method for estimating the fraction of mineral dust in particulate matter using PM2.5-to-PM10 ratios. Particuology, 28(5), 114-120, 2015.

9. Qingyu, G. , Fuchun, L. , Liqin, Y. , Rui, Z. , Yanyan, Y. , and Haiping, L.: Spatial-temporal variations and mineral dust fractions in particulate matter mass concentrations in an urban area of northwestern China. Journal of Environmental Management, 222, 95-103, 2018.

10. Hidy, G.: Remote sensing of particulate pollution from space: have we reached the promised land?. Air Repair, 59(6), 642-644, 2009.

11. Prados, A. I. , Kondragunta, S. , Ciren, P. , and Knapp, K. R.: Goes aerosol/smoke product (GASP) over north America: comparisons to AERONET and MODIS observations. Journal of Geophysical Research, 112(D15), D15201, 2007.

12. Gao, L. , Li, J. , Chen, L. , Zhang, L. , and Heidinger, A. K.: Retrieval and validation of atmospheric aerosol optical depth from AVHRR over China. IEEE Transactions on Geoscience and Remote Sensing, 54(11), 1-12, 2016.

13. Levy, R. C. , Mattoo, S. , Munchak, L. A. , Remer, L. A. , Sayer, A. M. , and Hsu, N. C.: The collection 6 MODIS aerosol products over land and ocean. Atmospheric Measurement Techniques Discussions, 6(1), 159-259, 2013.

14. Hu, X. , Waller, L. A. , Lyapustin, A. , Wang, Y. , and Liu, Y.: Estimating ground-level PM2.5 concentrations in the Southeastern United States using MAIAC AOD retrievals and a two-stage model. Remote Sensing of Environment, 140, 220–232, 2014.

15. Ou, Y. , Chen, F. , Zhao, W. , Yan, X. , and Zhang, Q.: Landsat 8-based inversion methods for aerosol optical depths in the Beijing area. Atmospheric Pollution Research, 8(2), 267-274, 2017.

16. Sayer, A. M. , Hsu, N. C. , Bettenhausen, C. , and M.-J. Jeong.: Validation and uncertainty estimates for MODIS collection 6 "Deep Blue" aerosol data. Journal of Geophysical Research: Atmospheres, 118, 2013.

17. Xinpeng, T. , Sihai, L. , Lin, S. , and Qiang, L.: Retrieval of aerosol optical depth in the arid or semiarid region of northern Xinjiang, China. Remote Sensing, 10(2), 197, 2018.

18. Arvani, B. , Pierce, R. B. , Lyapustin, A. I. , Wang, Y. , and Teggi, S.: Seasonal monitoring and estimation of regional aerosol distribution over Po valley, northern Italy, using a high-resolution MAIAC product. Atmospheric Environment, 141, 106-121, 2016.

19. Wang, Z. , Chen, L. , Tao, J. , Zhang, Y. , and Su, L.: Satellite-based estimation of regional particulate matter (PM) in Beijing using Vertical-and-RH correcting method. Remote Sensing of Environment, 114(1), 50-63, 2010.

20. Jung, C. R. , Hwang, B. F. , and Chen, W. T.: Incorporating long-term satellite-based aerosol optical depth, localized land use data, and meteorological variables to estimate ground-level PM 2.5, concentrations in Taiwan from 2005 to 2015. Environmental Pollution, 237(2018), 1000-1010, 2017.

21. Chiou-Jye, H. , and Ping-Huan, K.: A deep CNN-LSTM model for particulate matter (PM2.5) forecasting in smart cities. Sensors, 18(7), 2220, 2018.

22. Li, X. , Peng, L. , Yao, X. , Cui, S. , Hu, Y. , and You, C. , et al.: Long short-term memory neural network for air pollutant concentration predictions: method development and evaluation. Environmental Pollution, 231, 997-1004, 2017.

23. Zhou, X. , and Chen, H.: Impact of urbanization-related land use land cover changes and urban morphology changes on the urban heat island phenomenon. Science of The Total Environment, 635, 1467-1476, 2018.

24. Jiao, L. , Xu, G. , Xiao, F. , Liu, Y. , and Zhang, B.: Analyzing the impacts of urban expansion on green fragmentation using constraint gradient analysis. The Professional Geographer, 1-14, 2017.

25. Li, L. , Yang, J. , and Wang, Y.: An improved dark object method to retrieve 500m-resolution AOT (aerosol optical thickness) image from MODIS data: a case study in the pearl river delta area, China. ISPRS Journal of Photogrammetry and Remote Sensing, 89, 1-12, 2014.

26. Su, T. , Li, Z. , and Kahn, R.: Relationships between the planetary boundary layer height and surface pollutants derived from lidar observations over China. Atmospheric Chemistry and Physics Discussions, 18(21), 1-38, 2018.

27. Cai, H. , Gui, K. , and Chen, Q.: Changes in haze trends in the Sichuan-Chongqing region, China, 1980 to 2016. Atmosphere, 9(7), 277, 2018.

28. Bao, G. , and Zeng, Z.: Multistability of periodic delayed recurrent neural network with memristors. Neural Computing and Applications, 23(7-8), 1963-1967, 2013.

29. Weninger, F. , Geiger, Jürgen, WöLlmer, M. , Schuller, B. , and Rigoll, G.: Feature enhancement by deep LSTM networks for ASR in reverberant multisource environments. Computer Speech and Language, 28(4), 888-902, 2014.

30. Srivastava, S. , and Lessmann, S.: A comparative study of LSTM neural networks in forecasting day-ahead global horizontal irradiance with satellite data. Solar Energy, 162, 232-247, 2018.